Nonstatistical Translational Energy Distribution of H_2 Elimination Products from $Co^+(^3F_4)$ + Propane

Emily L. Reichert† and James C. Weisshaar*

Department of Chemistry, University of Wisconsin-Madison, Madison, Wisconsin 53706-1396

Received: October 10, 2001; In Final Form: March 25, 2002

The velocity map imaging technique is applied to mass-selected $CoC_2H_4^+ + CH_4$ and $CoC_3H_6^+ + H_2$ elimination products from the $Co^+(^3F_4)$ + propane reaction studied under crossed-beam conditions at 0.19 eV collision energy. For both products, we obtain the joint scattering probability distribution $P(E,\Theta)$, where E and Θ are the product translational energy and scattering angle. Both angular distributions are forward-backward symmetric and only modestly anisotropic. Both product translational energy distributions $P(E)$ are in fairly good agreement with earlier results of Bowers and co-workers, indicating that the earlier distributions were dominated by reaction of ground-state Co^+. The fraction of the total available energy deposited into product translation is 0.13 for CH_4 and 0.44 for H_2. For CH_4 products, $P(E)$ is cold and would be readily fit by orbiting-transition-state phase-space theory (OTS−PST) without an exit-channel barrier. Evidently, incipient $CoC_2H_4^+ + CH_4$ products equilibrate in the $Co^+(C_2H_4)(CH_4)$ exit-channel well, from which they decay statistically. In sharp contrast, for H_2 products $P(E)$ exhibits a substantial hot, nonstatistical tail toward high energy, extending to the limits of the available energy. Although it is imaginable that the H_2 channel has a late potential energy barrier some 0.5 eV above products, we view this as highly unlikely. Instead, we suggest that the potential energy from an earlier multi-center transition state $MCTS_{H_2}$ is funneled efficiently, and highly nonstatistically, into product translation, although $MCTS_{H_2}$ is far from product-like. We believe that H_2 escapes on the same time scale as intramolecular vibrational redistribution (IVR) due to its light mass, the early potential energy *decoupling* of the migrating H atom from the incipient alkene moiety, and the weak kinetic energy coupling across the massive Co^+ ion. This surprising conclusion seemingly applies to H_2 products for the entire family of reactions of the late-3d series transition metal cations Fe^+, Co^+, and Ni^+ with alkanes.

I. Introduction

Over the past two decades, gas-phase transition metal cation chemistry with hydrocarbons has been the subject of intensive experimental and theoretical research.[1−3] The reactions of Fe^+, Co^+, and Ni^+ with propane, which break CH and CC bonds at low energy to form H_2 and CH_4 elimination products, have been particularly thoroughly studied.[4−21] Experimental efforts have employed ion beams and collision cells,[5−7,10−12,14,15] ion cyclotron resonance mass spectrometers,[4,8] fast-flow reactors,[9] and tandem mass spectrometers,[12−14] all with the goal of elucidating the lowest energy pathways to H_2 and CH_4 and the heights of key potential barriers.

As electronic structure methods strive for accurate prediction of reaction pathways and transition state energies in organometallic systems,[22] model gas-phase reactions serve as important benchmarks.[18,19,23,21] For M^+ + propane, density functional theory (DFT), most often in its B3LYP version,[24,25] has predicted surprising new mechanistic pathways.[16,18,19,21] Insertion into CC and CH bonds is energetically facile, not rate-limiting, and M^+ preferentially attacks the two weakest bonds of propane, the CC and secondary CH bonds. The lowest energy pathways are *concerted*, involving passage over rate-limiting *multi-center transition states* (MCTSs), in contrast to the stepwise mechanisms postulated earlier.[12,14] Using B3LYP results for key intermediates and transition states, we recently constructed statistical RRKM[26−28] rate models on the lowest energy adiabatic potential energy surfaces for elimination of H_2 and CH_4 from Co^+ and Ni^+ + propane.[18,19,21] By lowering the computed energies of the key MCTSs by 2−7 kcal/mol, we could explain a wide variety of experimental data including the time-resolved branching fractions measured in our crossed-beam experiment, Armentrout's reaction cross sections vs collision energy,[14,15] and H/D isotope effects on cross sections and branching fractions. Consistent with DFT energetics, the model invokes only one path to H_2 elimination involving *secondary* CH insertion and passage over $MCTS_{H_2}$ and one path to CH_4 elimination involving CC insertion and passage over $MCTS_{CH_4}$.

The only set of data that has resisted explanation are the H_2 product translational energy distributions $P(E)$.[12,14] For reactions of Fe^+, Co^+, and Ni^+ with propane, $P(E)$ for the CH_4 product is cold and readily explained by orbiting transition state-phase space theory (OTS−PST)[29,30] with no exit-channel barrier. In contrast, $P(E)$ for H_2 elimination is double-peaked and far *hotter* than can be explained by OTS−PST. In addition, H/D isotopic substitution has highly specific effects on $P(E)$; deuteration at the *secondary* hydrogens or perdeuteration diminishes the high energy tail, while *primary* deuteration affects $P(E)$ very little.[12,14]

Contamination of the earlier $P(E)$ measurements by excited electronic states M^{+*} might have caused the hot, nonstatistical energy tail for H_2 products.[18,19,21] Therefore, we decided to combine our state-specific crossed-beam apparatus with the new velocity map imaging technique[31,32] to determine $P(E,\Theta)$ for H_2 from exclusively ground-state $Co^+(^3F_4)$ + propane. Here,

* To whom correspondence should be addressed. E-mail: weisshaar@chem.wisc.edu.

† Current address: Arthur D. Little Co., Cambridge, Massachusetts.

10.1021/jp0137827 CCC: $22.00
Published on Web 05/17/2002

P(E,Θ) is proportional to the differential reactive scattering cross section in energy space, with Θ the scattering angle. Although not double-peaked, our distributions agree qualitatively with Bowers' earlier measurements.[12] In particular, the nonstatistical, high-energy tail persists. This helps to place the entire family of P(E) measurements,[33,12,14] including the intriguing H/D isotope effects, on more solid ground.

A natural suggestion is that H_2 products receive their high translational energy from a late potential energy barrier.[12,14] However, there is almost surely no barrier beyond the exit-channel complex $Co^+(C_3H_6)(H_2)$. We therefore suggest that the dynamics from $MCTS_{H_2}$ to products is "semi-direct,"[12,14] with H_2 often escaping before complete intramolecular vibrational energy redistribution (IVR) can occur. Thorough examination of this idea suggests that the key feature may be the structure and mass distribution within $MCTS_{H_2}$. The migrating hydrogen has already broken its CH bond with the propyl group; the heavy Co^+ atom sits between the incipient H_2 and propylene units. The resulting isolation of H_2 from propylene in terms of both kinetic and potential energy coupling may allow chemical reaction to compete with IVR despite the complexity of the system.[34,35]

If this surprising conclusion is correct, the bimodal P(E) for H_2 products arises not from two different reaction paths, but from the distribution of outcomes on a single, secondary CH bond insertion path.[36] We can thus retain the statistical model that explains so much data for Co^+ and Ni^+ + propane.[18,19,21] However, a puzzle remains in the remarkable pattern of H/D isotope effects on P(E).[12,14] Detailed understanding will require further electronic structure calculations augmented by classical trajectories on suitable model potential surfaces.

II. Experiment

Several publications have described the crossed-beam experiment and its usual operating parameters.[37,17,19] A detailed report of our implementation of the velocity map imaging technique has been published elsewhere;[38] a brief summary is provided here. As shown schematically in Figure 1, three pulsed beams cross in space and time in the ion extraction region of a time-of-flight mass spectrometer (TOF-MS): a skimmed atomic Co beam formed by laser ablation and seeded in Ar; a pseudo-skimmed, neat propane beam (Matheson >99.9%); and an ionizing dye laser beam (10 ns fwhm, <250 μJ/pulse) that creates Co^+ reactants by resonant two-photon ionization at a sharply defined $t = 0$.

Two ionization schemes were used in this study. Absorption of two photons at 32 028 cm^{-1} creates Co^+ exclusively in the ground spin−orbit level ($^3F_4$) via the $y^4G^\circ_{7/2} \leftarrow a^4F_{9/2}$ transition.[39] In a second scheme, absorption of two photons at 39 649 cm^{-1} via the $x^4D^\circ_{7/2} \leftarrow a^4F_{9/2}$ transition[39] creates Co^+ ions in an unknown distribution of electronic states with excitation energy as high as 1.7 eV. The $x^4D^\circ_{7/2}$ intermediate state has the nominal configuration $3d^74s4p$. Our earlier work suggests it will have strong propensity to preserve core configuration on ionization.[40−43] Thus, we expect the second scheme produces Co^+ primarily in the a^5F ($3d^74s$) state at 0.515 eV and the b^3F ($3d^74s$) state at 1.298 eV, but it could also include the terms a^1D ($3d^8$, 1.445 eV), a^3P ($3d^8$, 1.655 eV). We loosely refer to this indeterminate distribution of reactant states as Co^+*. The product mass spectrum from the Co^+* + propane reaction lacks $CoC_3H_8^+$ adduct ions, so we know that ground-state Co^+ is a minority species in the beam.

Bimolecular Co^+-propane collisions begin at $t = 0$ and continue to occur for 4 μs after the laser pulse, at which time ions are extracted for mass analysis by application of a high-voltage pulse to the ion extraction plates. The 101 cm long field-free flight tube is held at ground. The upper two of the three plates have open apertures to create an electrostatic ion lens, the purpose of which is to focus ions with the same transverse components of velocity (v_x, v_y) to the same point on the imaging ion detector.[31] Adjusting the ratio of voltages applied to the lower two extraction plates focuses the electrostatic ion lens.

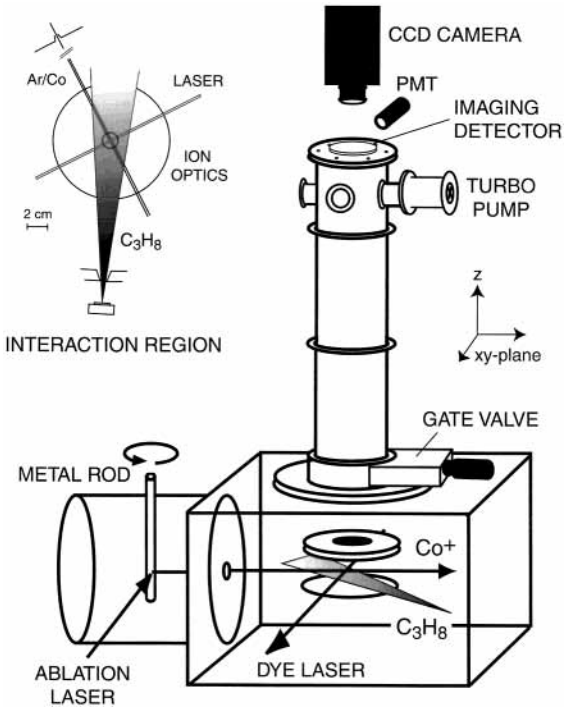

Figure 1. Schematic of crossed-beam, velocity map imaging apparatus. Inset shows top view of the interaction region. See text for details.

The imaging detector assembly (Galileo 3040-FM) consists of dual 40 mm diameter microchannel plates coupled to a fast (P47) phosphor screen and a coherent fiber-optic bundle that transmits the light image out of the vacuum chamber. A macro camera lens (Nikon, 50 mm, f/1.25) collects and focuses the light emitted by the bundle onto a UV-enhanced, liquid-nitrogen cooled CCD camera (Princeton Instruments LN/CCD-1300PB, 1340 × 1300 pixels, 16 bit, 20 μm × 20 μm pixel size). Images are transferred from the CCD camera to a computer and summed using WinView32 software (Princeton Instruments). As described earlier,[38] we use a thresholding algorithm provided with the software to discriminate against low levels of stray light that would otherwise obscure the product ion signal over long integration times.

Time-of-flight (TOF) mass spectra can be obtained by positioning a photomultiplier tube (Hamamatsu) above the fiber-optic bundle, where it views light from the phosphor screen directly. Mass spectra for the Co^+ + propane reaction are shown in Figure 2. The upper trace (Figure 2a) shows the products of the ground-state reaction; the lower trace (Figure 2b) shows the products of the reaction of excited-state Co^+* ions with propane. The decay time of the phosphor (nominal 80 ns to 10% of peak height) broadens the peaks to 100 ns fwhm at arrival times of 20 μs. Mass selection of products in the images is achieved by pulsing the lower microchannel plate voltage (DEI GRX-3.0K−H, <45 ns rise time) for a narrow time window of ±100 ns around the TOF of interest. The mass gate used to collect the $CoC_3H_6^+$ (+ H_2) product images is indicated in Figure 2a. The actual mass resolution is better than suggested by the photomultiplier trace in the figure. Spectra recorded with

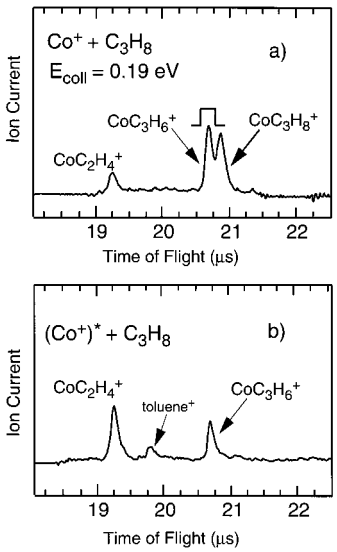

Figure 2. Product time-of-flight (TOF) mass spectrum from (a) $Co^+ + C_3H_8$ and (b) $Co^{+*} + C_3H_8$, both at 0.19 eV. The mass gate used for imaging $CoC_3H_6^+$ (+ H_2) is indicated in the upper trace (a).

a microchannel plate detector prior to implementing velocity map imaging show peaks of 40 ns fwhm without exponential tails (Figure 1 of ref 21). The 200 ns wide gate in fact selects $CoC_3H_6^+$ quite cleanly.

The technique produces a two-dimensional (2D) image of the velocity distribution of mass-selected product ions from which the full three-dimensional (3D) distribution can be extracted using an inverse Abel transform.[44] The typical product images presented below are summations of some 80 000 shots acquired over 160 min but transferred to and summed in the computer every 100 shots to minimize spatial coincidences. All of the product images show the raw data. However, we found it necessary to use a simple low pass filter algorithm[45] to smooth the images prior to analysis. Smoothed data are shown in all cross-sections of the product data for comparison with our best least-squares fits.

III. Results and Image Analysis

A. Velocity Map Images. A composite velocity map of the reactant beams and the resulting center-of-mass (CM) distribution is shown in Figure 3. As before,[38] the propane beam velocity distribution is probed by seeding it with 1−2% toluene and ionizing the toluene by R2PI at 37 480 cm^{-1}.[46] The Co^+ and toluene$^+$ signals must be scaled to account for their different arrival times as described below. The superimposed Newton diagram shows the most probable reactant, CM, and relative velocity vectors derived in the analysis procedure.[38] Reactants Co^+ or Co^{+*} and propane collide at a 150° angle as indicated by their laboratory frame velocity vectors $\mathbf{v}_{Co^+}$ and $\mathbf{v}_{pro}$. The near coincidence of the most probable CM velocity computed from the reactant beams and the most probable product velocities for both H_2 and CH_4 elimination provides a check against substantial velocity slip of the heavier toluene relative to propane.

In Figures 4 and 5, we present raw velocity map images of the H_2 and CH_4 elimination products of the ground-state $Co^+(^3F_4) + C_3H_8$ reaction at 0.19 eV collision energy. In Figure 6, an image of the H_2 elimination product from the reaction of excited-state $Co^{+*} + C_3H_8$ at 0.19 eV collision energy is shown. Adduct ions $CoC_3H_8^+$ move with velocity $\mathbf{v}_{CM}$ in the lab. Elimination of H_2 or CH_4 from this long-lived complex yields

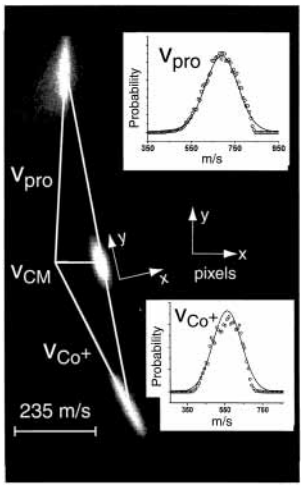

Figure 3. Unsmoothed velocity map images of the Co^+ and propane reactant beams scaled for flight times. Newton diagram shows most probable velocities. CM distribution is calculated from the reactant beam images. Original pixel coordinate system and rotated coordinate system of the CM distribution are indicated. Cross-sections through the long axis of each reactant beam image are shown with best-fit function. See text for details.

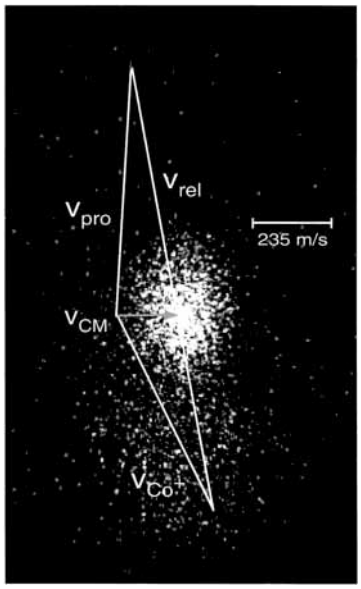

Figure 4. Unsmoothed velocity map image with mass gate set to the H_2 elimination product $CoC_3H_6^+$ (from Co^+). Superimposed Newton diagram shows $\mathbf{v}_{pro}$, $\mathbf{v}_{rel}$, $\mathbf{v}_{CM}$, and $\mathbf{v}_{Co^+}$, the propane, relative, center-of-mass, and Co^+ ion velocity vectors, respectively.

ionic products $CoC_3H_6^+$ (Figures 4 and 6) and $CoC_2H_4^+$ (Figure 5), whose images are centered on the tip of the center-of-mass vector.

The signal level for the ground-state Co^+ + propane reaction is extremely low; we detect only 0.2 ions/shot. Previous studies[15,21] place the reaction efficiency at 6−8% of the Langevin cross section[47] at ∼0.2 eV collision energy. Of this small fraction of successful collisions, the CH_4 elimination channel (Figure 5) makes up only 15% of all products, H_2 elimination (Figure 4) is 42%, and $CoC_3H_8^+$ is 43%.[21] The signal level is about 1.5 times greater for Co^{+*} + propane (Figure 6) with the number of reactant ions held constant. The TOF-MS of products from Co^{+*} shows branching in the ratio 3:2 for CH_4 and H_2 elimination, with no clear evidence of adducts. This indicates that the Co^{+*} beam is predominantly

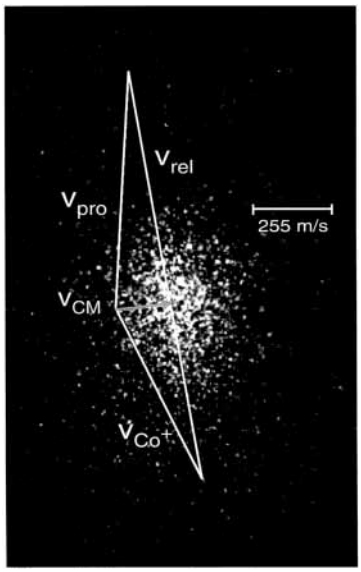

Figure 5. Unsmoothed velocity map image with mass gate set to the CH_4 elimination product $CoC_4H_4^+$ (from Co^+). Superimposed Newton diagram shows $\mathbf{v}_{pro}$, $\mathbf{v}_{rel}$, $\mathbf{v}_{CM}$, and $\mathbf{v}_{Co^+}$ as in Figure 4.

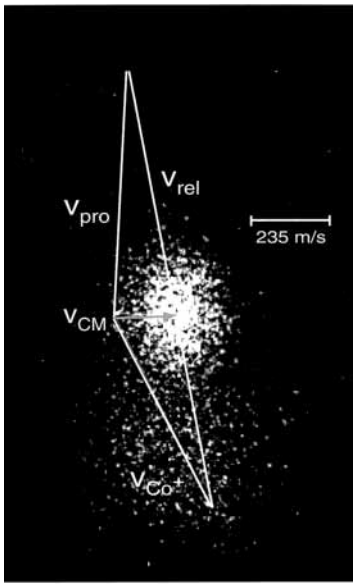

Figure 6. Unsmoothed velocity map image with mass gate set to the H_2 elimination product $CoC_3H_6^+$ (from Co^+*). Superimposed Newton diagram shows $\mathbf{v}_{pro}$, $\mathbf{v}_{rel}$, $\mathbf{v}_{CM}$, and $\mathbf{v}_{Co^+}$ as in Figure 4.

an excited-state beam, although we do not know its distribution over states (section II).

As in the earlier study of Co^+ + isobutane,[38] each product image contains a significant number of background product ions arising from reaction of the directed metal ion beam with the steady-state background pressure of propane in the chamber. The background (some 15% of the desired product signal) is the diffuse set of ions symmetrically placed about $\mathbf{v}_{Co^+}$. As before, we collect background-only images, fit them to a single 2D Gaussian, and strip their contribution from the product images prior to applying the Abel transform.

To a first approximation, the kinematics explain why the $CoC_2H_4^+$ (+ CH_4) products are distributed over a wider range of velocities than the $CoC_3H_6^+$ (+ H_2) products. The estimated exothermicity for $CoC_3H_6^+$ + H_2 channel is 16 kcal-mol^{-1} somewhat smaller than that for the $CoC_2H_4^+$ + CH_4 channel 24 kcal-mol^{-1}.[21] By conservation of linear momentum, the light H_2 acquires 98.1% of the relative velocity of the separating products $CoC_3H_6^+$ + H_2, leaving only 1.9% for the ion. For $CoC_2H_4^+$ + CH_4, the ion acquires 15.5% of the relative velocity.

B. Image Analysis. Our method of recovering three-dimensional (3D) velocity distributions from the $CoC_3H_6^+$ and $CoC_2H_4^+$ product images involves analytical inverse Abel transformation of a sum of 2D Gaussian functions fit to the raw data, a generalization of recent work on spherical distributions from photodissociation products.[48] First, nonlinear least-squares fits to velocity map images of the reactant beams are used to calculate the distribution of center-of-mass (CM) velocities $f_{CM}(x,y)$. Then the smoothed product image is fit to obtain $f_{prod}(x,y)$ as a sum of 2D Gaussian functions, from which the CM distribution is deconvolved analytically. Finally, the resulting 2D function $f(x,y)$ is inverse Abel transformed to yield the 3D function $I(x,y,z)$. Conversion of velocities to energies yields the probability distribution $P(E,\Theta)$, which is proportional to the differential reactive scattering cross section in energy space.[49] This can be appropriately integrated over Θ or E to yield the product translational energy distribution $P(E)$ and the product angular distribution $T(\Theta)$ in the CM frame.

We determine the quantitative velocity scale by least-squares fit of the intense portion of the experimental Co^+ and the isopropane images (Figure 3) to a single 2D Gaussian each, with the origin, orientation, and width parameter in each dimension as adjustable parameters.[50] Isopropane was imaged by R2PI[46] of a trace amount of toluene seeded into the beam. A consistency check described below ensures that velocity slip of the heavier toluene is unimportant. The weak "smearing" of the toluene image is due to poor spatial focusing of the wings of the pseudo-skimmed beam; this feature is stripped from the data as detailed elsewhere.[50] The intersection of the long axes of the best-fit Gaussians for the two reactant beams yields the velocity origin, reproducible to within ± 2 pixels (± 2 m−s^{-1}) across multiple data sets.

To convert vectors in pixel space to velocity vectors, we use the equation

$$\mathbf{v} = \mathbf{s}\frac{\delta}{M(\mathrm{TOF})} \qquad (1)$$

where **s** is a position vector in pixel space with origin determined as above, δ is a magnification factor due to the camera lens, M is a magnification factor due to the ion lens, and TOF is the time-of-flight for a particular ion. We obtain δ experimentally and M from the Simion model, as described in detail elsewhere.[50] Overall, the scale factor δ/M(TOF) becomes 1.18 ± 0.02 m−s^{-1}-pixel^{-1} for the $CoC_3H_6^+$ product and 1.27 ± 0.02 m−s^{-1}-pixel^{-1} for the $CoC_2H_4^+$ product. The individual images in Figure 3 have been transformed to include the scale factors so that all components are on a common velocity map. The most probable velocities are 560 ± 15 m−s^{-1} for the Co^+ beam and 690 ± 15 m−s^{-1} for the toluene-seeded propane beam (Table 1). These new measurements of the most probable beam velocities are in good agreement with less accurate values previously measured using a fast ion gauge, 580 ± 50 m−s^{-1} for Co^+ and 760 ± 100 m−s^{-1} for neat propane.[21] The reactant beam velocities and their intersection angle of 151 ± 1° yield the CM collision energy E = 0.19 ± 0.06 eV; here the uncertainty propagates the fwhm of the two reactant beams (Table 1). The earlier value for Co^+ provides an independent check on the magnification of the ion lens.

The properly scaled reactant beam distributions are convolved to give the distribution of CM velocities (Figure 3), which is

TABLE 1: Reactant and CM Lab Frame Velocity Distribution Characteristics[a]

species	v_{mp}[b]	Δv_x[c]	Δv_y[c]
Co^+	557 ± 14	29 ± 2	187 ± 10
Propane[d]	688 ± 15	35 ± 1	173 ± 12
CM[e]	159 ± 3	38 ± 1	123 ± 5

[a] All values in units of $m-s^{-1}$. Error reported as described in the text. [b] Most probable velocity. [c] Fwhm in the *x* or *y* direction. [d] Propane velocity distribution measured by R2PI of a trace amount of toluene seeded into the beam. [e] Calculated from convolution of Co^+ and propane velocity distributions derived from their velocity map images.

calculated point by point from the best-fit reactant Gaussians. This distribution is well fit by a single 2D Gaussian which yields the most probable CM speed of 159 ± 3 $m-s^{-1}$ in the lab frame (Table 1). The fwhm is 125 $m-s^{-1}$ along *y* and 40 $m-s^{-1}$ along *x*. The rotation angle for the long axis of the CM distribution is −18.0 ± 1.0° relative to the camera pixels (± two standard deviations of the mean for six data sets). Importantly, this coincides closely with the angle of −14.0 ± 1.0° for the axis of the most probable $\mathbf{v_{rel}}$ computed from the most probable reactant velocities. This coincidence, which allows application of the inverse Abel transform, arises from the particular shape and orientation of our beam distributions. As a counterexample, consider the convolution of a delta function with an elliptical distribution.

The product images of Figures 4−6 are fit to a sum of 2D Gaussians using nonlinear least squares with all data equally weighted.[45] The background-only image is fit to a single Gaussian whose shape is frozen and stripped from the signal-plus-background fits. We experimented extensively with the number and flexibility of the Gaussians used for the desired product signal.[50] For both the CH_4 and the H_2 elimination products, the final result used two Gaussians to fit the products (plus the single background Gaussian). We write the final fitting function in a 2D Cartesian CM velocity frame whose *y* axis coincides with the longer axis of the product distribution

$$f_{\text{prod}}(x,y) = \sum_{i=1}^{n} a_i \exp[-(x - x_0)^2/(2\sigma_{x,i}^2)] \times \exp[-(y - y_0)^2/(2\sigma_{y,i}^2)] \quad (2)$$

Here, *x* stands for v_x and *y* stands for v_y in the natural coordinate system of the products. The orientation of both Gaussians is fixed at −14° relative to the original pixel system to match the CM orientation. The adjustable fitting parameters include the amplitudes a_i, the independent widths along *x* and *y*, and the common origin (x_0, y_0). This function enforces forward−backward symmetry and cylindrical symmetry about the *y* axis, which nearly coincides with the most probable v_{rel}. Relaxing the symmetry constraints about each axis decreases the χ^2 figure of merit typically by about 10%, indicating only mild asymmetry in the data.

In Figures 7−9, we compare the smoothed data for the elimination products $CoC_3H_6^+$ from Co^+ and Co^+* and $CoC_2H_4^+$ from Co^+ to the best-fit function for cross-sections along v_x and v_y in the rotated (CM) coordinate frame. Each cross-section passes through the peak of the distribution. The background Gaussian is seen most easily as the off-center contribution in the v_y cross sections. The relative amplitudes and widths of the two Gaussians representing the product functions of Figures 7−9 are listed in Table 2. These mean values of the fitting parameters from 2 or 4 data sets are used to extract the product energy and angular distributions. The

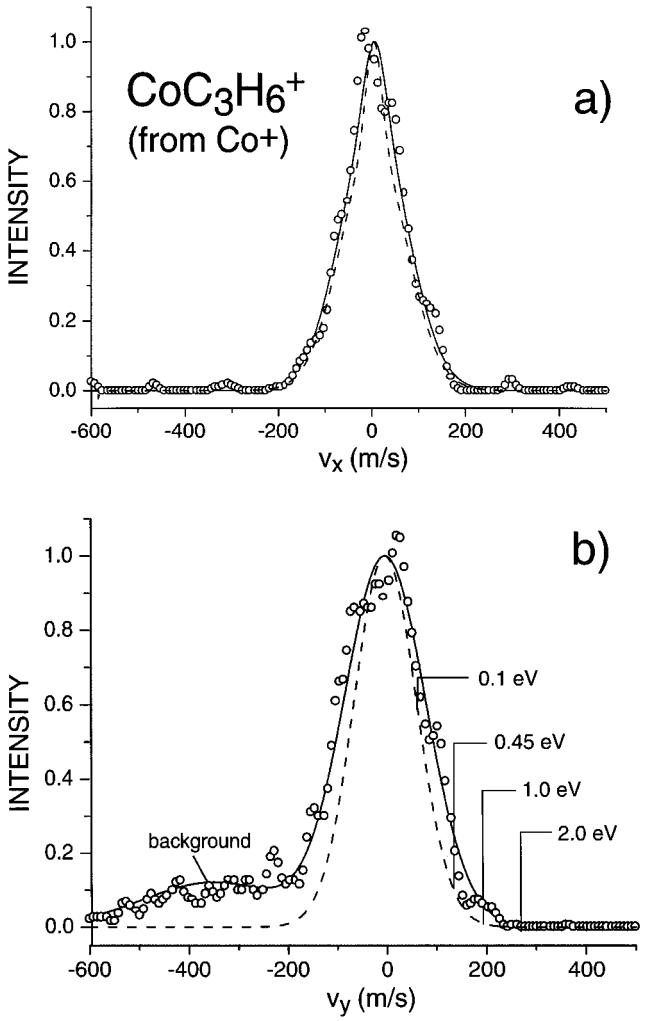

Figure 7. Smoothed $CoC_3H_6^+$ product intensity (from ground-state Co^+) shown as cross-sections along v_x (top) and v_y (bottom) in the rotated CM coordinate system. Solid lines are best nonlinear least-squares fits $f_{prod}(x,y)$. Dashed line in lower trace shows deconvolved product function $f(x,y)$. Along v_x, $f(x,y)$ and $f_{prod}(x,y)$ are essentially superimposable. Relative product translation energies correspond to the deconvolved velocity function (dashed line).

uncertainties listed for each parameter in the table are ± two standard deviations of the mean of the best-fit parameters when the data were grouped into four sets (H_2 from ground-state Co^+). When the data were grouped into two sets due to low signal-to-noise (H_2 and CH_4 data from excited-state Co^+), the parameter uncertainties are ± the range covered by the two fits. Many of the parameters are not as sharply defined as in the earlier Co^+ + isobutane study.[38] Typically, the product Gaussian of larger width, which determines the high-energy tail of P(*E*), is quite robust across data sets, whereas the narrower Gaussian varies substantially. Accordingly, the average energy and fwhm of the P(*E*) distribution are better determined than the most probable (peak) energy.

It is significant that for both products, the best-fit common origin of the two product Gaussians (x_0,y_0) agrees with the most probable CM value calculated from the reactant images within ± 17 $m-s^{-1}$ (± 14 pixels). This can be compared to the dispersion in the product origins, which is ± 5 $m-s^{-1}$ (± 4 pixels) for $CoC_2H_4^+$ and ± 7 $m-s^{-1}$ (± 6 pixels) for $CoC_3H_6^+$ and with that for the most probable CM value, ± 3 $m-s^{-1}$ (± 3 pixels). This consistency check provides reassurance that the measured toluene$^+$ distribution from the

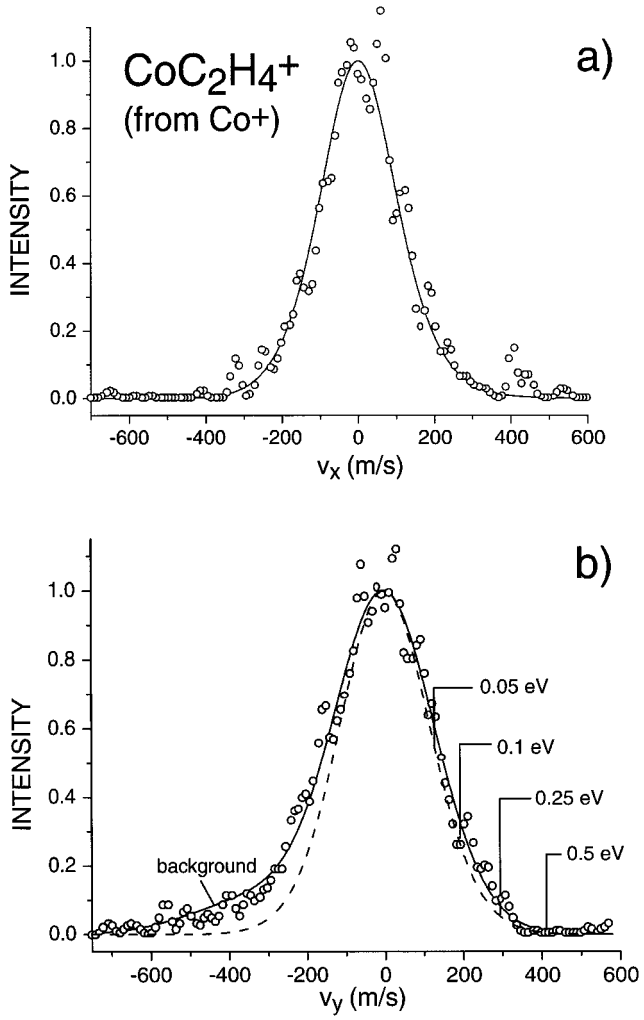

Figure 8. Smoothed $CoC_2H_4^+$ product intensity (from ground-state Co^+) shown as cross-sections along v_x (top) and v_y (bottom) in the rotated CM coordinate system. Solid lines are best nonlinear least-squares fits $f_{prod}(x,y)$. Dashed line in lower trace shows deconvolved product function $f(x,y)$. Along v_x, $f(x,y)$ and $f_{prod}(x,y)$ are essentially superimposable. Relative product translation energies correspond to the deconvolved velocity function (dashed line).

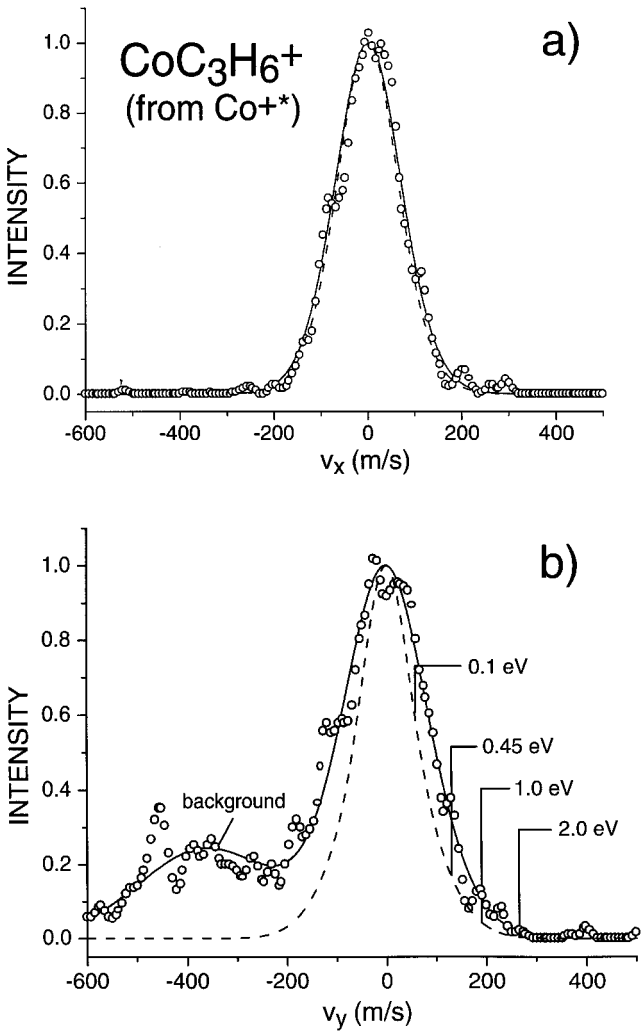

Figure 9. Smoothed $CoC_3H_6^+$ product intensity (from excited-state Co^{+*}) shown as cross-sections along v_x (top) and v_y (bottom) in the rotated CM coordinate system. Solid lines are best nonlinear least-squares fits $f_{prod}(x,y)$. Dashed line in lower trace shows deconvolved product function $f(x,y)$. Along v_x, $f(x,y)$ and $f_{prod}(x,y)$ are essentially superimposable. Relative product translation energies correspond to the deconvolved velocity function (dashed line).

seeded toluene/isopropane beam accurately reflects the actual isopropane distribution.

The CM velocity distribution $f_{CM}(x,y)$is deconvolved analytically from $f_{prod}(x,y)$ using the Fourier transform convolution theorem.[51] The resulting deconvolved 2D product function $f(x,y)$ is the input to the inverse Abel transform

$$f(x,y) = \sum_{i=1}^{2} a_i' \exp[-x^2/(2\sigma_{x,i}'^2)] \exp[-y^2/(2\sigma_{y,i}'^2)] \quad (3)$$

Here, x and y refer to v_x and v_y and i labels the components of the two Gaussians in $f_{prod}(x,y)$. The amplitudes a_i' are proportional to the amplitudes a_i in eq 2 and $\sigma_{x,i}'^2$ and $\sigma_{y,i}'^2$ are the deconvolved widths ($\sigma_{x,i}^2 - \sigma_{x,CM}^2$) and ($\sigma_{y,i}^2 - \sigma_{y,CM}^2$), in which the subscript "CM" refers to the fitted CM Gaussian widths.

Cross sections through f(x,y) are shown as the dashed line in Figures 7−9. Corresponding relative translational energies are indicated. The widths in the v_y direction of $f_{prod}(x,y)$ are reduced significantly more by the deconvolution than those along v_x due to the shape of the CM distribution, for which $\sigma_{y,CM}$ is about three times $\sigma_{x,CM}$ (Table 1). The uncertainties in the table are calculated as described above for $f_{prod}(x,y)$ over 2 or 4 data sets. The widths in the v_y direction of $f_{prod}(x,y)$ are reduced significantly more by the deconvolution than those along v_x due to the shape of the CM distribution, whose width in the y direction is about three times that in the x direction (Table 1). After deconvolution, both H_2 elimination distributions are nearly isotropic within the uncertainty of the parameters; the CH_4 distribution is slightly anisotropic (Table 2).

The deconvolved product function $f(x,y)$ is the integral of the desired 3D velocity distribution $I(x,y,z)$ along the z axis, which is perpendicular to the collision plane as shown in Figure 6. $I(x,y,z)$ is cylindrically symmetric about the y axis. The full 3D velocity distribution $I(r,y,\phi)$ is obtained by performing the inverse Abel transform at all y, where $x = r\sin\phi$, $z = r\cos\phi$, and $y = y$ in cylindrical coordinates. After conversion to spherical coordinates the distribution becomes

$$I(v,\Theta,\phi) = \sum_{i=1}^{2} [a_i'/(\sqrt{2\pi}\sigma_{x,i}')] \exp[-(v\sin\Theta)^2/(2\sigma_{x,i}'^2)] \times \exp[-(v\cos\Theta)^2/(2\sigma_{y,i}'^2)] \quad (4)$$

where $r = v\sin\Theta$ and $y = v\cos\Theta$ and $\phi = \phi$. Here, v is the

TABLE 2: Relative Amplitude and Fwhm Best-Fit Parameters for $CoC_3H_6^+$ and $CoC_2H_4^+$ Product Images[a]

	$CoC_3H_6^+ + H_2$ (from Co^+)		$CoC_3H_6^+ + H_2$ (from Co^{+}*)		$CoC_2H_4^+ + CH_4$ (from Co^+)	
	$f_{prod}(x,y)$[c]	$f(x,y)$[d]	$f_{prod}(x,y)$[c]	$f(x,y)$[d]	$f_{prod}(x,y)$[c]	$f(x,y)$[d]
$a_1/(a_{1+}\ a_2)$	0.24 ± 0.03	0.24 ± 0.03	0.41 ± 0.06	0.41 ± 0.06	0.46 ± 0.03	0.46 ± 0.03
$\Delta v_{x,1}$[b]	81 ± 31	71 ± 35	127 ± 16	121 ± 16	164 ± 40	159 ± 40
$\Delta v_{y,1}$[b]	175 ± 41	127 ± 52	165 ± 12	109 ± 27	255 ± 30	220 ± 33
$a_2/(a_{1+}\ a_2)$	0.76 ± 0.03	0.76 ± 0.03	0.59 ± 0.06	0.59 ± 0.06	0.54 ± 0.03	0.54 ± 0.03
$\Delta v_{x,2}$[b]	169 ± 1	165 ± 1	197 ± 22	193 ± 23	302 ± 14	301 ± 14
$\Delta v_{y,2}$[b]	211 ± 7	176 ± 14	240 ± 6	205 ± 11	347 ± 19	323 ± 21

[a] All widths are in units of product velocity in the CM frame, $m-s^{-1}$. [b] Fwhm in the *x* or *y* direction. [c] Mean values of best-fit parameters for each product image (eq 2), errors reported as described in the text. [d] Mean values of parameters of the product functions from which the CM has been deconvolved.

magnitude of the product CM velocity vector in 3D space, and Θ is the scattering angle between the initial and final relative velocity vectors. $P(v,\Theta) = v^2 I(v,\Theta,\phi)$ is the product velocity-angular distribution, which is proportional to the differential cross section in velocity space.[49] The distribution is converted from velocity space to energy space using $E = 1/2\mu v_{rel}'^2$, where μ is the reduced mass and $v_{rel}' = v(m_{total}/m_{neutral})$ is relative velocity of the separating ionic and neutral fragments. Here, $m_{neutral}$ is the mass of the neutral fragment CH_4 or H_2, and m_{total} is the total mass of the $CoC_3H_8^+$ complex. The result takes the form

$$P(E,\Theta) = \sqrt{E}\sum_{i=1}^{2} A_i \exp[-(E\sin^2\Theta)/(2\sigma''^2_{x,i})] \times \exp[-(E\cos^2\Theta)/(2\sigma''^2_{y,i})] \quad (5)$$

which is proportional to the differential cross section in energy space. Here, $A_i = a_i'/\sqrt{2\pi}\sigma''_{x,i}$, and the σ'' are the deconvolved widths expressed in energy units. From $P(E,\Theta)$ we obtain the angular distribution $T(\Theta)$ analytically by integration over E

$$T(\Theta) = \frac{\sqrt{\pi}}{2}\sum_{i=1}^{2} A_i[\sin^2\Theta/2\sigma''^2_{x,i} + \cos^2\Theta/2\sigma''^2_{y,i}]^{-3/2} \quad (6)$$

The product translational energy distribution $P(E)$[49] is obtained by integration over the solid angle $d\omega = 2\pi\sin\Theta d\Theta$. This result cannot be expressed analytically. In practice, we obtained $T(\Theta)$ and $P(E)$ by numerical integration of eq 5.

C. Product Translational Energy and Angular Distributions. Product translational energy distributions for the elimination products of the ground-state Co^+ + propane reaction at 0.19 eV collision energy are shown in Figures 10a and 11a. The $P(E)$ for the H_2 elimination from the Co^{+}* reaction is shown in Figure 10b. The solid curves show the most probable $P(E)$ calculated using the mean values of the $f(x,y)$ fitting parameters from Table 2. For each product distribution, the most probable energy E_{mp}, the fwhm ΔE, and the mean energy $\langle E\rangle$ are listed in Table 3. The dashed curves illustrate the range of $P(E)$ functions consistent with the data, estimated by simultaneously pushing each width parameter in $f(x,y)$ (Table 1) and also the pixel-velocity conversion factor of eq 1 over the range of their uncertainties. We show the "extreme" results from this procedure as dashed lines, in each case renormalized to unit area. This range reasonably depicts the variation among curves derived from individual data sets. As described in section III B, the $P(E)$ is most robust in the higher energy tail region, while there is more variability in the lower energy peak part of the distribution. For this reason, the pixel-velocity conversion factor error contributes 20−30% of the error in $\langle E\rangle$ and ΔE, but only 5−15% of the error reported for E_{mp}.

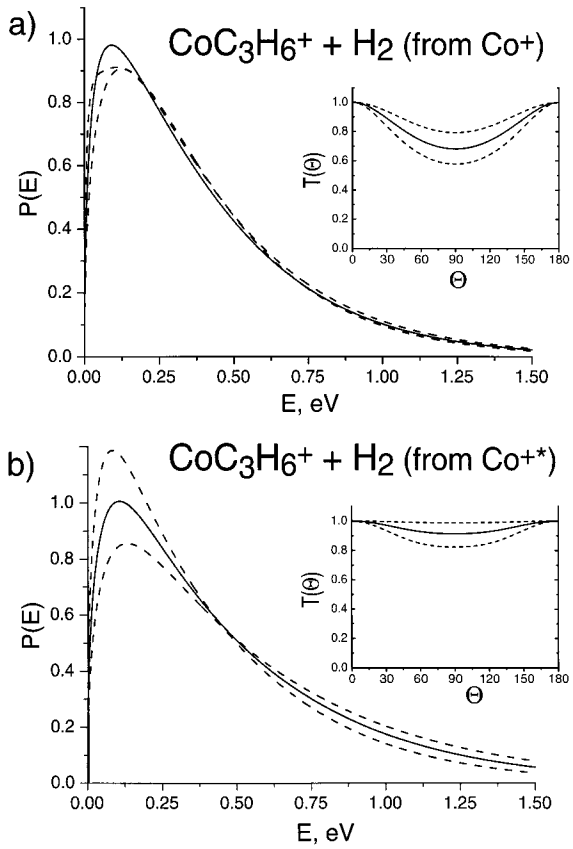

Figure 10. Translational energy distribution for the H_2 elimination products $CoC_3H_6^+$ from (a) the ground-state $Co^+ + C_3H_8$ reaction and from (b) the excited-state $Co^{+}* + C_3H_8$ reaction. Insets show angular distribution $T(\Theta)$ integrated over energy for each Θ. Dashed lines show uncertainty bounds estimated as described in text.

For the H_2 elimination product from ground-state Co^+ (Figure 10a), we find $E_{mp} = 0.091 \pm 0.034$ eV and $\langle E\rangle = 0.40 \pm 0.02$ eV, roughly 44% of the total available energy. The tail of the distribution extends substantially beyond 0.9 eV, the sum of the reaction exothermicity plus the mean collision energy of 0.19 eV. We will return to this point below. The distribution has $\Delta E = 0.44 \pm 0.05$ eV and falls to 10% of the maximum at 1.01 eV. The mean $P(E)$ curve in Figure 10a does not lie "between" the extreme error curves in the low energy region of the distribution. This is because the narrower, poorly determined Gaussian component becomes extremely narrow when its widths are pushed to the small side of the uncertainty range so that its contribution to the overall area of the $P(E)$ curve is greatly diminished.

The most probable $P(E)$ curves for H_2 elimination products from Co^+ and Co^{+}* are compared in Figure 10. The excited state curve has a significantly larger high-energy tail, but overall the two curves are quite similar. Quantitatively, $\langle E\rangle$ increases

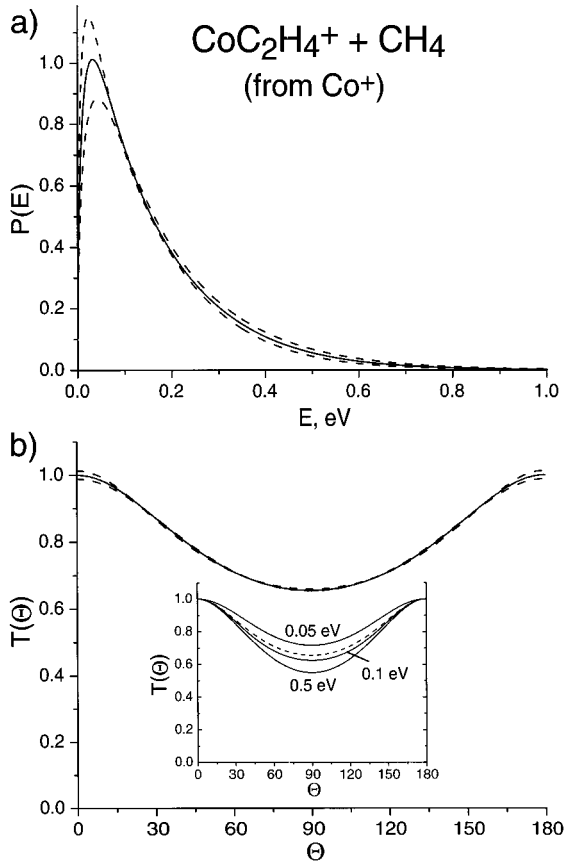

Figure 11. (a) Translational energy distribution for the CH_4 elimination product $CoC_2H_4^+$ from ground-state $Co^+ + C_3H_8$. Dashed lines show uncertainty bounds estimated as described in text. (b) Angular distribution $T(\Theta)$ integrated over energy for each Θ. Dashed lines show uncertainty bounds. Inset shows variation of $P(E,\Theta)$ with E as indicated; here the dashed line is $T(\Theta)$.

TABLE 3: Characteristics of P(E) for $CoC_3H_6^+$ and $CoC_2H_4^+$ Products

property (eV)	reactant state	$CoC_3H_6^+ + H_2$	$CoC_2H_4^+ + CH_4$	source
$\langle E\rangle^a$	$Co^{+\,d,g}$	0.40 ± 0.02	0.16 ± 0.02	this work
	$Co^{+}*\,^{e,g}$	0.50 ± 0.07		this work
	$(Co^+)^{f,h}$	0.33	0.099	ref 12
$E_{mp}{}^b$	$Co^{+\,d,g}$	0.091 ± 0.034	0.033 ± 0.010	this work
	$Co^{+}*\,^{e,g}$	0.11 ± 0.02		this work
	$(Co^+)^{f,h}$	0.09	0.024	ref 12
ΔE^c	$Co^{+\,d,g}$	0.44 ± 0.05	0.16 ± 0.03	this work
	$Co^{+}*\,^{e,g}$	0.51 ± 0.08		this work
	$(Co^+)^{f,h}$	0.28	0.075	ref 12

[a] Mean translational energy. [b] Most probable translational energy. [c] Fwhm of $P(E)$ distribution. [d] Ground spin−orbit state $^3F_4$ selected by R2PI. [e] Unknown distribution of excited states with 0.5−1.7 eV electronic energy; see section II. [f] Broad electronic state distribution in the range of 0.09−1.7 eV. $P(E)$ likely dominated by ground state (a^3F, 0.09 eV); see section IV A. [g] 0.19 eV collision energy. [h] Thermal distribution of collision energy near 300 K.

from 0.40 ± 0.02 eV for the reaction with Co^+ to 0.50 ± 0.07 eV for the reaction with Co^+*. The fwhm ΔE increases from 0.44 ± 0.05 eV to 0.51 ± 0.08 eV. The most probable energy E_{mp} increases from 0.09 ± 0.03 eV to 0.11 ± 0.02 eV. Overall, these shifts are quite modest and are only marginally significant within the uncertainty of the fitting.

For the CH_4 product (Figure 11a), we find $E_{mp} = 0.033 \pm 0.010$ eV and $\langle E\rangle = 0.16 \pm 0.02$ eV, roughly 13% of the total available energy. The fwhm is $\Delta E = 0.16 \pm 0.03$ eV; the distribution has fallen to 10% of the maximum at 0.41 eV. The

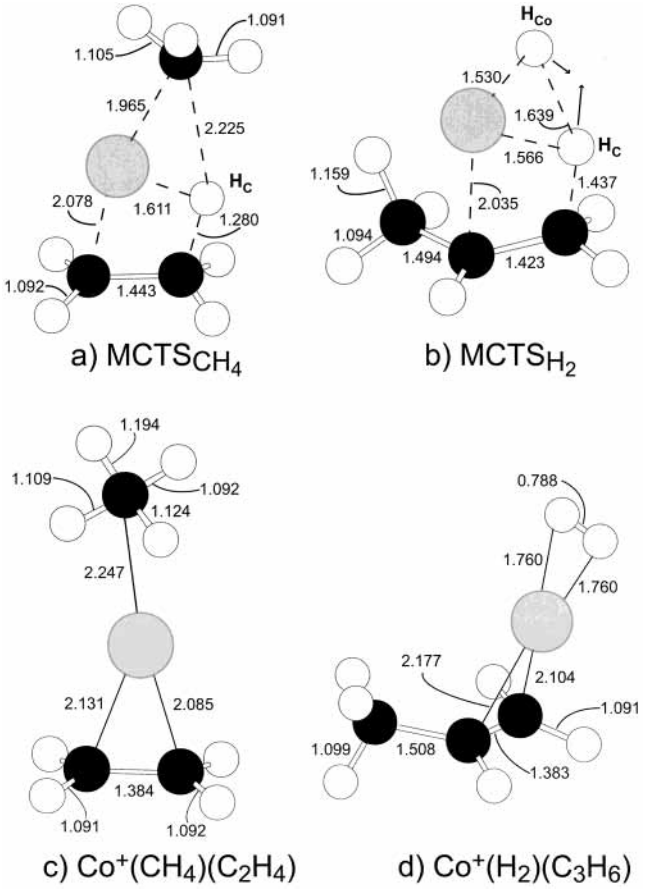

Figure 12. Geometries of multi-center transition states (from ref 21) and exit-channel complexes along CH_4 and H_2 elimination paths (our preliminary work, optimized at the B3LYP/Wachters+D95** level of theory). Distances in Å.

errors reported here again give the range of results on varying both fitting parameters and scale factor.

The H_2 product angular distributions $T(\Theta)$ from ground-state Co^+ and excited-state Co^+* are only mildly anisotropic (insets, Figures 10a and 10b). The $T(\Theta)$ for CH_4 elimination, which is more surely forward−backward peaked, is shown in Figure 11b. The solid lines are the most probable curves, whereas the dashed lines again represent error limits, as for $P(E)$. In all cases, the preferred function $P(E, \Theta)$ is not strictly separable into a product of angular and energy functions, as shown for the CH_4 product (inset to Figure 11b), but it is more nearly separable than in our earlier study of Co^+ + isobutane (Figure 9 of ref 38). The peak-to-valley ratios for the most probable distributions are 1.5 ± 0.3 for ground-state H_2 elimination (inset, Figure 10a), 1.1 ± 0.1 for excited-state H_2 elimination (inset, Figure 10b), and 1.51 ± 0.01 for CH_4 elimination (Figure 11b).

In our previous study of the Co^+ + isobutane reaction,[38] the CH_4 elimination $T(\Theta)$ showed stronger anisotropy. Approximating the transition state by the B3LYP exit channel complex structure $Co^+(CH_4)(C_3H_6)$, we found $T(\Theta)$ was well described by the collision complex model of Miller and co-workers,[52] which predicts that the dissociation of a prolate top along its symmetry axis should give rise to a distribution highly peaked at 0° and 180°. For Co^+ + propane, the B3LYP exit complex structure $Co^+(CH_4)(C_2H_4)$ is considerably more prolate (Figure 12) than in the Co^+ + isobutane case.[38] In general, we might expect H_2 products to be more isotropic than CH_4 products because a larger fraction of the initial orbital angular momentum must be channeled into product rotation due to the small reduced

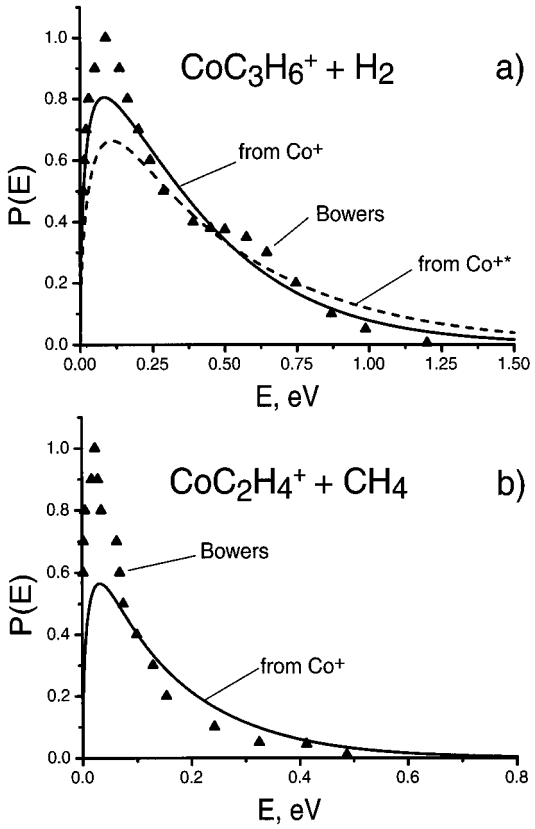

Figure 13. (a) Comparison of $P(E)$s for H_2 elimination (solid line for Co^+, dashed for Co^+* products) and (b) for CH_4 elimination (solid line) from this work with earlier work from the Bowers group (triangles, ref 12).

mass. This in turn allows H_2 to recoil with final orbital angular momentum vector tipped further away from the initial orbital angular momentum vector. In addition, CH_4 products from propane may be more isotropic than CH_4 from isobutane because they are less constrained to dissociate along the symmetry axis of the transition state due to reduced steric bulk.

IV. Discussion

A. Product Translational Energy Distributions. Product translational energy distributions for the Co^+ + propane reaction have been measured by Bowers and co-workers using tandem mass spectrometry.[12] In their experiment, Co^+ reactants are formed by 150 eV electron impact ionization of $Co(CO)_3NO$ in a source region containing 1 mTorr of propane reactant. Metastable $CoC_3H_8^+$ adducts formed at 300 K are extracted and mass-selected. They fragment in the second field free region of the mass spectrometer prior to energy analysis. In Figure 13, we compare the $P(E)$s from this work and those of the Bowers group for both the H_2 and CH_4 elimination channels. The distributions are shown with equal areas for ease of comparison. Quantitative parameters from the two sets of $P(E)$ measurements are compared in Table 3.

Qualitatively, for both CH_4 and H_2 the distributions from the two different experiments are quite similar. Comparing our ground-state H_2 elimination $P(E)$ to Bowers' data,[12] we see the two distributions peak at comparable energies and decay quite similarly at high energy. Bowers' H_2 distribution has $\langle E \rangle = 0.33$ eV, slightly lower than our ground-state distribution with $\langle E \rangle = 0.40 \pm 0.02$ eV. The Bowers CH_4 elimination distribution is more sharply peaked, with a fwhm $\Delta E = 0.075$ eV that is half of ours, $\Delta E = 0.16 \pm 0.03$ eV. Their distribution rises more sharply, and decays faster at high energy, with $\langle E \rangle = 0.099$ eV compared to 0.16 ± 0.02 eV from this work.

The H_2 elimination $P(E)$ from Bowers appears to be bimodal,[12] i.e., to have two peaks. A narrow, lower energy component peaks at ~0.1 eV and merges into a broad, higher energy component peaking at ~0.5 eV. We see no evidence of a double-peaked distribution for H_2 elimination in either the ground state or excited-state measurements from our experiment. We have checked that it is possible to synthesize such distributions from the fitting function of eq 2. The combination of a high amplitude narrow peak and a broader, low amplitude peak in the velocity distribution can indeed create this type of $P(E)$. However, our data do not support a double-peaked distribution.

In our earlier study of the Co^+ + propane reaction,[21] we suggested that the higher energy component of Bowers' H_2 elimination $P(E)$ might arise from the presence of excited-state reactants Co^+*. Electron impact on $Co(CO)_3NO$ at 50 eV creates 64% metastable Co^+* with additional energy in the range 0.5−1.7 eV relative to the ground state, according to ion chromatography studies.[13] The ions created by 150 eV electron impact in Bowers' Co^+ + propane study[12] probably include an even greater percentage of Co^+*. However, our $P(E)$ for H_2 elimination from pure ground-state Co^+ and the Bowers $P(E)$ are very similar (Figure 13a). The new results strongly suggest that products from excited electronic states did not contribute significantly to the earlier $P(E)$ for $Co^+ + C_3H_8$,[12] and by inference, for the other reactions in which double-peaked distributions were measured as well.[33,14] The reason is almost surely that complexes formed by M^+* are too short-lived to contribute within the time window of his experiment, 6−64 μs. In our much shorter average time window of 2 μs, we see no adducts in the Co^+* + propane TOF mass spectrum (Figure 2b) vs 43% adducts observed under the same conditions for the ground-state reaction (Figure 2a). Similar results have been reported by Bowers in ion chromatography studies of Co^+* and Fe^+* with propane,[13] in which the efficiency of complex collisional stabilization by He was found to be ~40 times less than in the ground-state reactions.

Our $P(E)$s for H_2 elimination from the reaction of Co^+ and Co^+* with propane (Figure 10) are remarkably similar considering the latter has additional available energy in the range 0.5−1.7 eV. Both curves peak at roughly the same energy (Table 3), but the high-energy tail extends somewhat further for Co^+* than for Co^+. The fraction of $P(E)$ that extends beyond 1.0 eV for the ground-state reaction is 0.07 ± 0.01, compared to 0.12 ± 0.05 for the excited-state reaction. The absence of adduct ions $CoC_3H_8^+$ on a 2 μs time scale after initiation of the collision suggests that Co^+* + C_3H_8 reactants access excited-state surfaces that either dissociate rapidly (perhaps in part due to a $4s^1$ configuration)[13] or live sufficiently long to make a nonradiative transition to the ground-state surface in the vicinity of the deep $Co^+(C_3H_8)$ well.[53] With additional internal energy of at least 0.5 eV, such complexes produce elimination products or decay back to reactants much faster than complexes from ground-state reactants. We return to the question of why $P(E)$ is so similar for Co^+ and Co^+* below.

The literature values for the reaction exothermicities are 0.71 eV for the H_2 channel and 1.04 eV for the CH_4 channel.[12] In our internally cold crossed-beam experiment with ground-state Co^+ selected by R2PI, in addition to the exothermicity only the collision energy of 0.19 ± 0.07 eV is available to our products. We expect negligible rotational and vibrational energy in the reactants.[54] We can use our product $P(E)$s from internally

cold reactants as a rough consistency check on the literature exothermicities. From the upper limit of 0.26 eV for our reactant translational energy distribution and the literature exothermicities, the maximum energy available to products would be 1.30 eV for CH_4 products and 0.97 eV for H_2 products. The form of the fitting functions guarantees that the tail of $P(E)$ is a sum of exponentially decaying functions of energy. The $P(E)$ for CH_4 has 99.99 ± 0.01% of the probability below 1.30 eV whereas the ground-state P(E) for H_2 has 93.0 ± 1.1% of the probability below 0.97 eV (Figures 10a and 11a). Inspection of the deconvolved velocity function $f(x,y)$ for H_2 in Figure 7 shows that it has little or no significant amplitude beyond the velocity corresponding to 1.0 eV. The new results thus seem quite consistent with the literature exothermicities.

Because Bowers' earlier $P(E)$ distribuion evidently arises from ground-state M^+, we now summarize the remarkable effects observed on H/D isotopic substitution. For the reactions of Fe^+, Co^+, and Ni^+ with propane,[12,14] and Co^+ with isobutane,[33] Bowers' $P(E)$ for H_2 appears double-peaked to varying degrees and exhibit a consistent pattern in the effect of deuteration at particular sites. For all three metal ions, deuteration of the *secondary* carbon in propane ($CH_3CD_2CH_3$) results in substantial cooling of the high-energy tail for the HD elimination $P(E)$ relative to the H_2 elimination P(E) from C_3H_8. In contrast, deuteration of both primary carbons ($CD_3CH_2CD_3$) has only a minor effect, seemingly concentrated in the low-energy peak when it appears at all. C_3D_8 behaves more like $CH_3CD_2CH_3$ than $CD_3CH_2CD_3$. For example, in Co^+ + propane $\langle E \rangle$ stays constant at 0.33 eV for H_2 elimination from C_3H_8 and for HD from $CD_3CH_2CD_3$, but decreases sharply to 0.24 eV for HD from $CH_3CD_2CH_3$ and for D_2 from C_3D_8. In Co^+ + isobutane,[33] the high-energy tail of $P(E)$ cools substantially upon deuteration of the *tertiary* carbon.

In summary, the CH_4 and H_2 product translational energy distributions from the ground-state Co^+ + propane reaction are quite different. On average the CH_4 products place only about 13% of the available energy for reaction into translation; for H_2, this becomes a remarkably large 44%. Given the real differences in experimental conditions, the new results are in reasonable agreement with those from the Bowers group,[12] who found their CH_4 elimination $P(E)$ could be fit by statistical phase space theory without a exit channel barrier, whereas their much hotter, double-peaked H_2 distribution could not be described in the same fashion. This appears to rule out the possibility that Bowers' $P(E)$s were contaminated by excited-state reactions.

B. Reaction Paths. Very recently, theoretical methods such as density functional theory (DFT) have begun to contribute significantly to mechanistic thinking about the reactions of Fe^+, Co^+, and Ni^+ with propane.[16,18,19,21] DFT (B3LYP) consistently finds that the lowest energy paths are *not* stepwise bond insertion, rearrangement to a σ-bonded intermediate, and elimination of molecular products as previously postulated. Rather, the lowest energy paths are *concerted* (Figure 14), leading directly from a bond insertion well over a *multi-centered transition state* (MCTS) to an exit-channel complex in which the products are almost completely formed.

According to DFT calculations,[16,18,19,21] at low collision energy both CH_4 and H_2 products arise from the initial formation of a $M^+(C_3H_8)$ complex. In the lowest energy H_2 elimination pathway, metal insertion into the weaker, *secondary* CH bond is followed by β-hydrogen migration over $MCTS_{H_2}$ to form the exit-channel complex $M^+(H_2)(C_3H_6)$, which subsequently fragments. The lowest energy pathway to CH_4 elimination involves initial CC bond insertion followed by β-hydrogen migration over

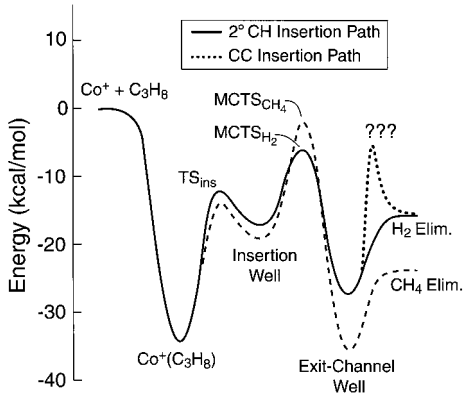

Figure 14. Schematic lowest energy pathways for the elimination of CH_4 and H_2 from $Co(CoC_3H_8)^+$ complexes. Only the secondary CH insertion path is shown for H_2. Relative energies based on B3LYP calculations except for the MCTS energies, which were adjusted to fit experimental data.

a different $MCTS_{CH_4}$ to form $M^+(CH_4)(C_2H_4)$, which then fragments to products. Stepwise pathways through rearrangement intermediates such as $M^+(H)_2(C_3H_6)$ and $M^+(H)(CH_3)(C_2H_4)$ are not found for Fe^+, Co^+, or Ni^+, which evidently lack sufficient bonding capacity. Pathways involving initial primary CH bond insertion lie at least 10 kcal/mol above those involving CC insertion (leading to CH_4 elimination), and 5−10 kcal/mol above those involving secondary CH insertion (leading to H_2 elimination). In all cases, *β-methyl* migrations are found to be prohibitively high in energy.

For the Co^+ and Ni^+ + propane reactions,[18,21] we have combined density functional electronic structure calculations of the properties of stationary points with statistical rate modeling of key rate-limiting steps. By simply adjusting the MCTS energies from B3LYP calculations downward by 2−7 kcal/mol, we were able to build rate models that explain reaction cross sections and elimination branching ratios vs collision energy,[14,15] absolute time scales for complex decay,[19,21] and deuterium isotope effects on cross sections[14,15] quite accurately. As a result of this approach, a rather comprehensive picture of the lowest energy reaction pathways leading to elimination of CH_4 and H_2 has been developed. The only experimental data not readily explained by the model are the H_2 product translational energy distributions.

For the reactions of Fe^+, Co^+, and Ni^+ + propane, the P(E)s for the CH_4 elimination channel are *colder* than predicted by orbiting transition state phase space theory (OTS−PST) with no exit-channel barrier.[12,14] OTS−PST was able to reproduce the narrow distributions when a tight transition state was placed along the reaction path, restricting the angular momentum available to products and thus diminishing the high energy component of the $P(E)$. The rate-limiting, tight transition state was proposed to be primary CH insertion,[12,14] but theory now shows it is $MCTS_{CH_4}$ instead.[16,18,21]

The H_2 elimination $P(E)$s from Fe^+, Co^+, and Ni^+ + propane are difficult to understand. In all cases, they are much hotter than OTS−PST can explain without an exit channel barrier.[12,14] For all three reactions, the Bowers $P(E)$ for H_2 is double-peaked,[12,14] whereas our $P(E)$ from Co^+ + propane is not. From here on, we loosely refer to the colder part of these distributions peaking at 0.05−0.10 eV as the "statistical part" and to the remaining, high-energy tail as the "nonstatistical part." In the original papers,[12,14] the H/D isotope effects were interpreted as evidence of two distinct, competitive reaction pathways for H_2 elimination: *primary* CH insertion (not shown in Figure 14)

giving rise to the statistical part of $P(E)$, and *secondary* CH insertion giving rise to the nonstatistical part. The experimental results and the assumption that the initial CH bond insertion was rate-limiting naturally suggested that the secondary CH insertion path produced hot, nonstatistical H_2 from a tight exit-channel transition state, whereas the primary insertion path produced statistical H_2 after equilibration in a late potential well.[12,14]

A decade later, we know much more about the reaction paths, primarily from DFT calculations. First, B3LYP consistently finds that the rate-limiting steps involve multi-center transition states (MCTSs), not CH or CC bond insertion.[16,18,21] As described in detail earlier,[15,18] isotope effects at the two relevant MCTSs are not straightforward, because one H and one D are moving in *both* MCTSs for *either* deuteration pattern. Second, B3LYP consistently finds that the MCTS following secondary CH insertion lies 5−10 kcal/mol *below* the MCTS following primary CH insertion,[16,18,21] so the latter path should not be competitive at the low collision energies of interest here. Indeed, for the Ni^+ and Co^+ + propane reactions we find no need for the primary CH insertion path in our statistical rate modeling, which invokes only a single, secondary CH insertion pathway to H_2 and a single, CC insertion pathway to CH_4.[18,21]

Because this simple, unifying model explains so much data, we must explore whether the secondary CH insertion pathway *alone* might give rise to the anomalous P(E) and the characteristic deuterium isotope effects.[12,14] For Fe^+, Co^+, and Ni^+, the deuterium isotope effects on $P(E)$ would then follow a simple rule. *Substantial reduction of the high-energy, nonstatistical tail of P(E) occurs on deuteration of the bond into which the metal ion initially inserts.* The colder, statistical peak in the distribution is hardly influenced at all by deuteration, regardless of site.

C. H_2 Exit-Channel Barrier or Non-Statistical Dynamics? The hot, nonstatistical H_2 translational energy distributions would normally suggest the presence of a late exit-channel barrier on the potential energy surface. The $P(E)$ of Figure 10a for H_2 from $Co^+ + C_3H_8$ extends to at least 1.0 eV. An extreme model for dissociation over a tight transition state would add the potential energy of the barrier to a statistical distribution of available energy in the reaction coordinate to yield a $P(E)$ that looks statistical but is shifted from $E = 0$ to $E_{barrier}$. A more realistical model would shade such a distribution back toward $E = 0$ to a degree depending on the competition between motion along the reaction path and intramolecular vibrational redistribution (IVR) of the available energy into other degrees of freedom.[55−57] According to these ideas, the observed P(E) in Figure 10a suggests a barrier height E_0 of at least 0.5 eV = 13 kcal/mol *above* $CoC_3H_6^+ + H_2$ products.

However, we see no reason the H_2 path should have a post-exit-complex barrier at all. DFT finds the exit-channel complex $Co^+(C_3H_6)(H_2)$ roughly 10−15 kcal/mol below their respective products. A *subsequent* 13 kcal/mol barrier becomes at least a 23 kcal/mol barrier when viewed from the $Co^+(C_3H_6)(H_2)$ well. Both the CH_4 and the H_2 exit-channel complexes are already quite product-like (Figure 12). Accordingly, the experimental $P(E)$ for the CH_4 channel can be explained quantitatively with no exit-channel barrier. It is very difficult to imagine what forces would create a tight transition state *beyond* the H_2 exit-channel complex. Accordingly, our preliminary DFT calculations on the closely related $Co^+ + C_2H_6$ system find no barrier on a C_{2v} symmetry path from the exit-channel complex $Co^+(C_2H_4)(H_2)$ to $CoC_2H_4^+ + H_2$ products.

In addition, a tight transition state just prior to H_2 products cannot readily explain the deuterium isotope effects on $P(E)$.[12,14] Differential zero-point effects would go in the direction of *increasing* the barrier height relative to products for the deuterated case, by perhaps 1−2 kcal/mol. As suggested earlier, it might still be possible to rationalize the isotope effects as arising from the change in time scale of departing HD or D_2 relative to H_2, with the heavier products allowing more time for IVR to act.[33] This effect goes in the right direction, but predicts that $P(E)$ should be the same for HD from $Co^+ + CH_3CD_2CH_3$ and $Co^+ + CD_3CH_2CD_3$, because both reactions go through very similar Co^+(ethylene)(HD) exit-channel complexes. Moreover, there should be a substantial additional effect of perdeuteration to make D_2 vs secondary deuteration to make HD, but the two $P(E)$s are similar.[12]

Lacking a conventional alternative, we now carefully explore the possibility that the hot H_2 products receive their kinetic energy from an earlier barrier on the potential energy surface, namely $MCTS_{H_2}$ (Figure 12).[12,14] The dynamics outward from $MCTS_{H_2}$ to products must then be "semi-direct,"[12,14] with only a fraction of the complexes becoming trapped and thermalized in the exit-channel well prior to dissociation. In this idea, the cold, statistical part of $P(E)$ is due to the thermalized complexes while the hot, nonstatistical part is due to complexes that escape without being completely thermalized. We interpret the broad distribution of product kinetic energy as indicative of a *distribution of outcomes* for reactive events following essentially the *same reaction path*, rather than a *branching* of reactive events between two different paths.[36]

On the basis of the adjusted barrier height at $MCTS_{H_2}$ of −0.3 eV that matches so much other experimental data[21] and the exothermicity of −0.71 eV,[12] $MCTS_{H_2}$ lies 0.41 ± 0.15 eV above products. Long-lived reactive complexes pass over this barrier with a statistical distribution of the additional available energy in the reaction coordinate that peaks near zero and extends to 0.56 eV in our experiment. Because the tail of the product $P(E)$ extends to at least 1.0 eV, this picture requires that conversion to product translation of both potential energy of $MCTS_{H_2}$ and kinetic energy along the reaction coordinate must be quite efficient. The fast H_2 must exit in $v = 0$, because $v = 1$ consumes 0.5 eV of energy. From Figure 10a, we estimate that perhaps 25% of the reactive complexes are trapped and thermalized to produce the narrow part of the distribution peaking near 0.1 eV.

There is some precedent for this idea in polyatomic systems from recent experimental studies and related classical trajectory calculations for gas-phase S_N2 reactions[58−60,55−57] and for condensed phase organic biradical rearrangements.[36] In these systems, the potential energy surface has a deep well between a key transition state and products. Classical trajectories indicate that the forces at the transition state and beyond in effect "aim" a subset of reactive complexes toward the product valley in such a way that they pass quickly through the well without equilibrating. However, in the case of Fe^+, Co^+, and $Ni^+ + C_3H_8$, the geometry of $MCTS_{H_2}$ is far from product-like (Figure 12), and the transition vector is *not* aiming complexes toward products.

Is this mechanism then plausible? First, we need to explain why H_2 products suffer only partial IVR, while CH_4 products are completely equilibrated. The reason may well lie in the structure and mass distribution in the two MCTSs and in the exit-channel complexes to which they lead (Figure 12). Beyond $MCTS_{H_2}$, the two hydrogen atoms are moving toward a geometry in which the H_2 molecule lies opposite propene, with

the heavy Co^+ ion in the middle. This isolation of the H_2 moiety may sharply diminish the rate of IVR. Lehmann, Pate, Scoles, and co-workers[34,35] have studied IVR from the fundamental and first overtone of the CH stretch for the sequence of molecules $(CH_3)_3CC{\equiv}CH$, $(CH_3)_3SiC{\equiv}CH$, and $(CH_3)_3SnC{\equiv}CH$. The IVR rate decreases a factor of 10−40 as the central carbon atom changes to silicon and an additional factor of 3 as silicon changes to tin. This strong "heavy-atom effect" is interpreted at least in part as "blocking" of complete IVR into the terminal methyl groups (which provide most of the state density) by the heavy central atom.[34,35] The hot (−C≡CH) side of the molecule drives the Si or Sn atom far above its natural frequencies, so kinetic energy coupling across the heavy atom is poor.

Something quite analogous may occur at $MCTS_{H_2}$ and just beyond. As seen in Figure 12, the migrating hydrogen initially bound to the primary carbon, which we call H_C, is already strongly bound to Co^+ at $MCTS_{H_2}$, with $r(Co^+{-}H_C) = 1.57$ Å. For comparison, the hydrogen originally bound to Co^+, which we call H_{Co}, has $r(Co^+{-}H_{Co}) = 1.53$ Å. The C−H_C bond is mostly broken at $MCTS_{H_2}$, with $r(C{-}H_C) = 1.44$ Å compared with 1.09 Å for a normal CH bond. Evidently as the H_2 bond energy is beginning to be released, the migrating hydrogen H_C has already broken its bond to the incipient propene moiety, i.e., potential energy coupling from H−H to the other side of the molecule is weak. IVR must occur primarily through the heavy Co atom, to which both hydrogens have potential energy coupling that is strong at $MCTS_{H_2}$ but diminishes toward the exit-channel complex as H_2 pulls away from Co^+. The kinetic energy coupling is extremely weak; the mass ratio between hydrogen and Co is much smaller than in the substituted acetylene examples.[34,35] This is a somewhat different explanation for nonstatistical decay than those provided in other examples.

The CH_4 products may completely equilibrate for several reasons. The geometries of Figure 12 show that $MCTS_{CH_4}$ is significantly "earlier" than $MCTS_{H_2}$. In particular, $r(C{-}H_C)$ is 0.15 Å shorter, providing stronger potential energy coupling that can bypass the heavy Co^+. In addition, the incipient CH_4 provides more local internal degrees of freedom to which energy can be easily transferred than the incipient H_2. Excitation of internal rotation and bending motions of methane may quickly steal energy from the reaction coordinate after passage over $MCTS_{CH_4}$, analogous to the rapid heating of the (−C≡CH) side of the acetylenic molecules.[34,35] The larger mass of CH_4 compared with H_2 then provides much better kinetic energy coupling through the Co^+ atom. Finally, the 8-fold more massive CH_4 departs the complex with three times slower velocity than H_2 for the same relative kinetic energy, allowing more time for IVR to compete.[33]

In this picture, the sensitivity of $P(E)$ for HD to the exact pattern of deuterium substitution (primary CD vs secondary CD)[12,14] is remarkable and potentially quite revealing. As argued above, this cannot simply involve the change in time scale for departure of hydrogen for H_2 vs HD vs D_2. Judging from the geometry of $MCTS_{H_2}$ (Figure 12), we anticipate that its potential energy is funneled initially into motion of H−H. The early decoupling of H_C from its carbon atom isolates much of the released energy on one side of the complex, regardless of the exact details of the subsequent motion. We expect motion of the H−H moiety relative to $Co^+(C_3H_6)$ in the exit-channel complex to be quite soft, so that as H_2 forms it has enough energy to sample local bending vibrations and internal rotations. Now recall that deuteration of the wagging hydrogen (now D_{Co}) cools $P(E)$ substantially, while deuteration of the migrating hydrogen (D_C) affects $P(E)$ very little, whether the wagging hydrogen is H or D. Evidently, certain dynamical events that control $P(E)$ occur *before* H_{Co} and H_C have had time to interconvert by internal rotation, although further details are not easily intuited. Perhaps deuteration of the wagging hydrogen enhances energy transfer across Co, substantially cooling P(E). Or perhaps it alters trajectories as they "turn a corner" toward the exit well, causing them to convert more potential energy to motion transverse to the reaction path. In any event, the translationally hot H_2 must ultimately be vibrationally cold, because $v = 1$ consumes 0.5 eV.

The rough coincidence of the 0.4 eV height of $MCTS_{H_2}$ relative to products and the energy of the second peak in the Bowers $P(E)$ at 0.5 eV (Figure 13a) is intriguing. Assuming the time delay in the Bowers experiment filters out excited-state contributions (section IV A), the internal energy of the complexes is actually 0.15 eV lower on average in his experiment than in ours. Perhaps the additional internal energy in our experiment broadens the nonstatistical part of $P(E)$ toward lower energy, filling in the trough between Bowers' two peaks. This idea is congruent with the surprising similarity of the $P(E)$s for H_2 from our pure ground-state Co^+ beam and the unknown, 0.5−1.7 eV distribution of excited states in the Co^{+}* beam (Figure 10b). This suggests that complexes from Co^{+}* + propane have reached the ground-state potential energy surface long before they form products. Again, the additional energy does not couple efficiently into product translation. If it frequently populated $H_2(v = 1)$, as the geometry of $MCTS_{H_2}$ might suggest, the excess internal energy would add probability to $P(E)$ in the range 0−0.5 eV or so.

Can we extend the idea of nonstatistical energy release from $MCTS_{H_2}$ for the reactions of Fe^+, Co^+, and Ni^+ with propane to reactions with larger alkanes? It appears so. The experimental story for Co^+ + isobutane is very similar in both the shape of $P(E)$ and the deuterium isotope effects;[33,38] deuteration of the *tertiary* CH bond cools $P(E)$ substantially in direct analogy to the propane result. Isobutane behaves like propane with one secondary hydrogen mutated to become a methyl group.[61,38]

The cases of Co^+ and Ni^+ + *n*-butane provide rather different examples of efficient coupling of MCTS potential energy to H_2 product translation. From collision-induced dissociation studies and H/D isotope effects, we know that the $MC_4H_8^+$ product ions are primarily $M(C_2H_4)_2^+$ in both cases, and 1,4 elimination predominates.[33] Accordingly, for Ni^+ + *n*-butane, Blomberg and Siegbahn[23] found that the lowest energy path to H_2 involves initial insertion in the central CC bond (again the weakest bond in the molecule) and passage over a unique, nearly symmetric MCTS in which two hydrogens are migrating toward each other while the two incipient ethylenes rotate into place. Now the vibrational motion along the reaction coordinate involves the two hydrogens moving toward each other and slightly away from the Ni^+ center. It is easy to envision this motion evolving smoothly into product translation, which should enhance escape vs IVR. However, the migrating hydrogens are less isolated; they are less strongly bound to Ni^+ and more strongly bound to the primary carbons than their counterparts in the M^+ + propane examples. Accordingly, the shape of $P(E)$ is qualitatively different.[33] It decreases slowly and approximately linearly from $E = 0$ to about 0.8 eV and then decays roughly exponentially to the highest energy observed, about 1.4 eV. There is no evidence of a low energy, statistical peak; the deuterium isotope effects are much more modest than in propane.[33]

Finally, we must explain why *both* H_2 and CH_4 products from the early-3d series metals Ti^+ and V^+ + C_3H_8 exhibit cold,

statistical P(*E*)s,[62] in sharp contrast to the behavior of H_2 from the late metals Fe^+, Co^+, and Ni^+.[12,14] This may well be due to necessary spin changes during the course of the reaction for Ti^+ and V^+. The ground states have high-spin configurations unsuitable for bond insertion: $Ti^+(3d^24s, {}^4F)$ and $V^+(3d^4, {}^5D)$. As discussed earlier,[41,43] in order to insert they must access attractive, low-spin potentials (doublet for Ti^+, triplet for V^+) correlating to excited states of the reactant metal ion and leading to the CH or CC bond insertion wells. The spin argument is cleaner in V^+ + propane, for which it is clear from theory that a second spin change is necessary to reach ground-state, quintet $VC_3H_6^+ + H_2$ products. For the closely related $VC_2H_4^+$ species, theory finds the quintet structure some 15 kcal/mol below the triplet structure.[63] This second spin change should be slow because it likely occurs in the vicinity of the exit-channel well and involves a substantial geometry change. Triplet $VC_3H_6^+(H_2)$ must convert to quintet $VC_3H_6^+(H_2)$, which subsequently dissociates to quintet products with statistical *P*(*E*).[62] The argument is less compelling for Ti^+ + propane, because it is likely that doublet $TiC_3H_6^+ + H_2$ lies slightly below quartet $TiC_3H_6^+ + H_2$.[64] However, the quartet surface evidently dips down below the doublet at the exit-channel complex geometry. A second spin change *could* occur there, delaying the departure of H_2 and defeating the possibility of semi-direct dynamics past $MCTS_{H_2}$.

V. Conclusions

Our measurement of H_2 and CH_4 product translational distributions from exclusively ground-state Co^+ + propane corroborates the results of earlier work.[12] The CH_4 products have statistical *P*(*E*)s, while the H_2 products have much hotter, nonstatistical *P*(*E*). Evidently the reactions of ground-state Fe^+, Co^+, and Ni^+ with propane have qualitatively similar *P*(*E*)s which respond similarly to selective deuteration.[12,14] On the basis of earlier statistical rate models built upon DFT calculations of stationary point properties,[18,19,21] we believe that at low total energy all of the H_2 products arise from a single reaction path leading from secondary CH insertion over $MCTS_{H_2}$ to the exit-channel well. By the process of elimination, we suggest that the dynamics beyond $MCTS_{H_2}$ efficiently funnel potential energy into product translation. The key feature seems to be the isolation of the light H_2 moiety on the opposite side of the heavy Co^+ atom from the alkene and the early decoupling of the migrating H from the incipient propene. Inefficient kinetic and potential energy coupling thus slow the IVR rate sufficiently to allow departure of H_2 to compete with energy equilibration.[34,35] Similar events may occur in essentially all reactions of late-3d series metal cations with alkanes to produce molecular hydrogen. By carrying out DFT calculations along the intrinsic reaction coordinate connecting $MCTS_{H_2}$ to the exit channel $Co^+(C_2H_4)(H_2)$, we can learn how geometry evolves as the potential energy is released. This may shed further light on the remarkable H/D isotope effects.[12,14]

Acknowledgment. We thank the National Science Foundation (NSF-0071458) and the donors of the Petroleum Research Fund (Grant No. 33441-AC6) for generous support of this research. Prof. Fleming Crim and Dr. David Chandler made helpful suggestions. Dr. Gert Thurau helped with the early implementation of the experiment. We also thank Dr. Meredith Porembski for calculating the B3LYP exit complex and transition state structures reported in this paper.

References and Notes

(1) Eller, K.; Schwarz, H. *Chem. Rev.* **1991**, *91*, 1121.
(2) Weisshaar, J. C. Control of Transition Metal Cation Reactivity by Electronic State Selection. In *State-Selected and State-to-State Ion−Molecule Reaction Dynamics*; Ng, C. Y., Ed.; Wiley & Sons: New York, 1992.
(3) Armentrout, P. B.; Baer, T. *J. Phys. Chem.* **1996**, *100*, 12 866.
(4) Byrd, G. D.; Burnier, R. C.; Freiser, B. S. *J. Am. Chem. Soc.* **1982**, *104*, 3565.
(5) Halle, L. F.; Houriet, R.; Kappes, M. M.; Staley, R. H.; Beauchamp, J. L. *J. Am. Chem. Soc.* **1982**, *104*, 6293.
(6) Halle, L. F.; Armentrout, P. B.; Beauchamp, J. L. *Organometallics* **1982**, *1*, 963.
(7) Houriet, R.; Halle, L. F.; Beauchamp, J. L. *Organometallics* **1983**, *2*, 1818.
(8) Jacobson, D. B.; Freiser, B. S. *J. Am. Chem. Soc.* **1983**, *105*, 5197.
(9) Tonkyn, R.; Ronan, M.; Weisshaar, J. C. *J. Phys. Chem.* **1988**, *92*, 92.
(10) Georgiadis, R.; Fisher, E. R.; Armentrout, P. B. *J. Am. Chem. Soc.* **1989**, *111*, 4251.
(11) Schultz, R. H.; Armentrout, P. B. *J. Am. Chem. Soc.* **1991**, *113*, 729.
(12) van Koppen, P. A. M.; Brodbelt-Lustig, J.; Bowers, M. T.; Dearden, D. V.; Beauchamp, J. L.; Fisher, E. R.; Armentrout, P. B. *J. Am. Chem. Soc.* **1991**, *113*, 2359.
(13) van Koppen, P. A. M.; Kemper, P. R.; Bowers, M. T. *J. Am. Chem. Soc.* **1992**, *114*, 10 941.
(14) van Koppen, P. A. M.; Bowers, M. T.; Fisher, E. R.; Armentrout, P. B. *J. Am. Chem. Soc.* **1994**, *116*, 3780.
(15) Haynes, C. L.; Fisher, E. R.; Armentrout, P. B. *J. Phys. Chem.* **1996**, *100*, 18300.
(16) Holthausen, M. C.; Koch, W. *Helv. Chim. Acta* **1996**, *79*, 1939.
(17) Noll, R. J.; Yi, S. S.; Weisshaar, J. C. *J. Phys. Chem.* **1998**, *102*, 386.
(18) Yi, S. S.; Blomberg, M. R. A.; Siegbahn, P. E. M.; Weisshaar, J. C. *J. Phys. Chem.* **1998**, *102*, 395.
(19) Yi, S. S. Effects of Angular Momentum Conservation on Reactions of Co^+ and Ni^+ with Alkanes: Experiment and Statistical Theory. Doctoral Dissertation, University of Wisconsin-Madison, 1998.
(20) Fedorov, D. G.; Gordon, M. S. *J. Phys. Chem. A* **2000**, *104*, 2253.
(21) Yi, S. S.; Reichert, E. L.; Weisshaar, J. C.; Holthausen, M. C.; Koch, W. *Chem. Eur. J.* **2000**, *6*, 2232.
(22) Koch, W.; Hertwig, R. H. Density Functional Theory Applications to Transition Metal Problems. In *Encyclopedia of Computational Chemistry*; Schleyer, P., Ed.; John Wiley: New York, 1998; Vol. 1; p 689.
(23) Blomberg, M. R. A.; Siegbahn, P. E. M.; Yi, S. S.; Noll, R. J.; Weisshaar, J. C. *J. Phys. Chem. A* **1999**, *103*, 7254.
(24) Becke, A. D. *J. Chem. Phys.* **1993**, *98*, 1372.
(25) Stephens, P. J.; Devlin, F. J.; Chabalowski, C. F.; Frisch, M. J. *J. Phys. Chem.* **1994**, *98*, 11 623.
(26) Robinson, P. J.; Holbrook, K. A. *Unimolecular Reactions*; Wiley-Interscience: New York, 1972.
(27) Gilbert, R. G.; Smith, S. C. *Theory of Unimolecular and Recombination Reactions*; Blackwell Scientific Publications: Oxford, U.K., 1990.
(28) Baer, T.; Hase, W. L. *Unimolecular Reaction Dynamics*; Oxford University Press: New York, 1996.
(29) Pechukas, P.; Light, J. C.; Rankin, C. *J. Chem. Phys.* **1966**, *44*, 794.
(30) Chesnavich, W. J.; Bowers, M. T. Stasitical Methods in Reaction Dynamics. In *Gas-Phase Ion Chemistry*; Bowers, M. T., Ed.; Academic Press: New York, 1979; Vol. 1.
(31) Eppink, A. T. J. B.; Parker, D. H. *Rev. Sci. Instrum.* **1997**, *86*, 3477.
(32) Parker, D. H.; Eppink, A. T. J. B. *J. Chem. Phys.* **1997**, *107*, 2357.
(33) Hanratty, M. A.; Beauchamp, J. L.; Illies, A. J.; van Koppen, P. A. M.; Bowers, M. T. *J. Am. Chem. Soc.* **1988**, *110*, 1.
(34) Lehmann, K. K.; Pate, B. H.; Scoles, G. *J. Chem. Phys.* **1990**, *93*, 2152.
(35) Thkerstel, E. R.; Lehmann, K. K.; Mentel, T. F.; Pate, B. H.; Scoles, G. *J. Phys. Chem.* **1991**, *95*, 8282.
(36) Carpenter, B. K. *J. Am. Chem. Soc.* **1996**, *118*, 10329.
(37) Noll, R. J. Bimolecular collisions in real time: Gas-phase reactions of Co^+ and Ni^+ with hydrocarbons. Doctoral Dissertation, University of Wisconsin-Madison, 1994.
(38) Reichert, E. L.; Thurau, G.; Weisshaar, J. C. *J. Chem. Phys.* **2001**, *submitted for publication*.
(39) Sugar, J.; Corliss, C. *J. Phys. Chem. Ref. Data* **1985**, *14*, Suppl. 2.
(40) Sanders, L.; Hanton, S. D.; Weisshaar, J. C. *J. Phys. Chem.* **1987**, *91*, 5145.
(41) Sanders, L. Chemistry of Electronic State-Selected Gas-Phase Transition Metal Cations with Small Hydrocarbons. Doctoral Dissertation, University of Wisconsin-Madison, 1988.
(42) Sanders, L.; Hanton, S. D.; Weisshaar, J. C. *J. Chem. Phys.* **1990**, *92*, 3498.
(43) Sanders, L.; Hanton, S. D.; Weisshaar, J. C. *J. Chem. Phys.* **1990**, *92*, 1990.

(44) Bracewell, R. N. *Two-Dimensional Imaging*; Prentice-Hall: Englewood Cliffs, NJ, 1995.
(45) Press, W. H.; Flannery, B. P.; Teukolsky, S. A.; Vetterling, W. T. *Numerical Recipes: The Art of Scientific Computing*; Cambridge Univerisity Press: Cambridge, U. K., 1986.
(46) Lu, K.-T.; Eiden, G. C.; Weisshaar, J. C. *J. Phys. Chem.* **1992**, *96*, 9742.
(47) Gioumousis, G.; Stevenson, D. P. *J. Chem. Phys.* **1958**, *29*, 294.
(48) Yoder, L. M.; Barker, J. R.; Lorenz, K. T.; Chandler, D. W. *Chem. Phys. Lett.* **1999**, *302*, 602.
(49) Levine, R. D.; Bernstein, R. B. *Molecular Reaction Dynamics and Chemical Reactivity*; Oxford University Press: New York, 1987.
(50) Reichert, E. L. Doctoral Thesis, U. Wisconsin-Madison, 2001.
(51) Jansson, P. A. *Deconvolution of Images and Spectra*; Academic Press: San Diego, 1997.
(52) Miller, W. B.; Safron, S. A.; Herschbach, D. R. *Discuss. Faraday Soc.* **1967**, *44*, 108.
(53) Porembski, M.; Weisshaar, J. C. *J. Phys. Chem. A* **2001**, submitted for publication.
(54) Gallagher, R. J. Internal Energy Relaxation in Gases. Doctoral Dissertation, Yale University, 1972.
(55) Mann, D. J.; Hase, W. L. *J. Phys. Chem. A* **1998**, *102*, 6208.
(56) Su, T.; Wang, H.; Hase, W. L. *J. Phys. Chem. A* **1998**, *102*, 9819.
(57) Bolton, K.; Schlegel, H. B.; Hase, W. L.; Song, K. Y. *Phys. Chem. Chem. Phys.* **1999**, *1*, 999.
(58) Graul, S. T.; Bowers, M. T. *J. Am. Chem. Soc.* **1991**, *113*, 9696.
(59) Graul, S. T.; Bowers, M. T. *J. Am. Chem. Soc.* **1994**, *116*, 3875.
(60) DeTuri, V. F.; Hintz, P. A.; Ervin, K. M. *J. Phys. Chem. A* **1997**, *101*, 5969.
(61) Reichert, E. L.; Yi, S. S.; Weisshaar, J. C. *Int. J. Mass. Spectrom.* **2000**, *196*, 55.
(62) van Koppen, P. A. M.; Bowers, M. T.; Haynes, C.; Armentrout, P. B. *J. Am. Chem. Soc.* **1998**, *120*, 5704.
(63) Gidden, J.; van Koppen, P. A. M.; Bowers, M. T. *J. Am. Chem. Soc.* **1997**, *119*, 3935.
(64) Moc, J.; Fedorov, D. G.; Gordon, M. S. *J. Chem. Phys.* **2000**, *112*, 10247.